Energy Storage Materials 81 (2025) 104492

Contents lists available at ScienceDirect

Energy Storage Materials

journal homepage: www.elsevier.com/locate/ensm

Constructing vertical Li^+ transport "Highways" and interface regulation of composite solid electrolytes for ultra-stable lithium metal batteries

Zeyu Niu [a], Yuxuan Wang [a], Yang Wang [a], Yixin Wu [a], Ziqi Zhao [a], Guanghui Li [a], Jae-Kwang Kim [b], Xin Liu [a,*], Zexiang Shen [a], Minghua Chen [a,*], Stefano Passerini [c,d,e,*], Zhen Chen [a,*]

[a] Key Laboratory of Engineering Dielectric and Applications (Ministry of Education), School of Electrical and Electronic Engineering, Harbin University of Science and Technology 150080 Harbin, Heilongjiang, PR China
[b] Department of Solar & Energy Engineering, Cheongju University, Cheongju 28503 Chungbuk, Republic of Korea
[c] Helmholtz Institute Ulm (HIU), Helmholtzstrasse 11 89081 Ulm, Germany
[d] Karlsruhe Institute of Technology (KIT) 76021 Karlsruhe, Germany
[e] Austrian Institute of Technology (AIT), Center for Transportation Technologies, Giefinggasse 4 1210 Wien, Austria

ARTICLE INFO

Keywords:
3D interconnected composite solid electrolytes
Vertical ceramic framework
Multipath Li^+ transfer mechanism
Interface stability
Solid-state lithium metal batteries

ABSTRACT

Three-dimensional (3D) interconnected composite solid electrolytes (CSEs) hold significant promise for solid-state batteries by leveraging the combined strengths of ceramic and polymer electrolytes. However, optimizing ion transport in 3D-CSEs remains challenging, with unclear underlying mechanisms. Here, a CSE (marked as 3D-LATP) is developed by integrating 3D vertically aligned $Li_{1.3}Al_{0.3}Ti_{1.7}(PO_4)_3$ (LATP) framework with infiltrated poly(vinylidene fluoride-*co*-trifluoroethylene-*co*-chlorofluoroethylene) (P(VDF-TrFE-CFE)) and lithium bis(fluorosulfonyl)imide. The multipath Li^+ transfer mechanism and enhanced interfacial stability are thoroughly investigated. The vertically aligned LATP structure provides efficient ion transport "highways" and robust mechanical support. LATP also induces more generation of high dielectric constant β-crystalline phase in PVDF, thereby enhancing ionic transport kinetics at the ceramic/polymer interface. Strong LATP−N, N-dimethylformamide interactions enhance electrochemical stability with lithium metal. The high-dielectric polymer interlayer at the Li|CSE interface enables uniform Li^+ deposition, meanwhile significantly enhancing the safety property. As a result, compared to CSEs with an equal amount of randomly distributed LATP fillers, the 3D-LATP electrolyte demonstrates markedly improved ambient ionic conductivity, lithium-ion transference number, and critical current density. Li||$LiFePO_4$ full cells achieve an outstanding cycle lifetime of 2500 cycles (at 1 C rate), presenting a promising approach for designing high-performance CSEs that ensure efficient ion transport and stable interfaces.

1. Introduction

To meet the growing demand for energy storage in applications such as electric vehicles, energy grids, and electric aircrafts, it is essential to develop batteries that offer both high energy density and enhanced safety [1]. The flammability and instability of conventional liquid electrolytes pose severe risks such as thermal runaway and lithium dendrite growth, compromising the performance and safety of lithium-ion batteries [2]. Solid-state electrolytes (SSEs), with their excellent thermal stability and ability to suppress lithium dendrites, have emerged as a key focus of research, offering a promising solution to enhance battery safety and energy density [3]. Among the options, composite solid-state electrolytes (CSEs) are particularly considered as ideal candidates, chiefly due to their high ionic conductivity, excellent interfacial stability, superior ability to suppress lithium dendrite growth, good thermal stability, as well as their mechanical strength and flexibility [4].

Typically, zero-dimensional or one-dimensional fillers are embedded into a polymer matrix to improve ionic conductivity and mechanical strength of solid-state batteries [5]. However, inorganic particles tend to aggregate and become isolated within the polymer phase, which hinders the formation of fast and continuous lithium-ion transport channels [6].

* Corresponding authors.
E-mail addresses: liu.xin@hrbust.edu.cn (X. Liu), mhchen@hrbust.edu.cn (M. Chen), stefano.passerini@kit.edu (S. Passerini), chen.zhen@hrbust.edu.cn (Z. Chen).

https://doi.org/10.1016/j.ensm.2025.104492
Received 19 May 2025; Received in revised form 10 July 2025; Accepted 24 July 2025
Available online 24 July 2025

As a result, uneven lithium-ion flux develops at the Li|CSE interface, promoting lithium dendrite growth, ultimately causing rapid electrolyte degradation and a reduced cycle life [7]. In addition, CSEs incorporating dispersed particles lack stable structural support, making them more prone to deformation under high-temperature conditions, which raises potential safety concerns [8]. Inorganic fillers with three-dimensional (3D) framework can create continuous lithium-ion transport channels within the polymer electrolyte, enabling efficient lithium-ion transport through the polymer matrix, the inorganic framework, and the filler/-polymer interface [9]. This greatly improves ionic conductivity and addresses the issues with CSEs described above. Common synthetic methods investigated to date include freeze casting [10], sacrificial templating [11], and 3D printing [12]. Zhang et al. [13] fabricated a $Li_7La_3Zr_2O_{12}$ (LLZO) framework featuring uniformly aligned vertical pores using a cellulose template, which was subsequently infused with polyethylene oxide (PEO) to successfully construct a CSE. It has been revealed that lithium-ions were primarily transported through the interconnected LLZO phase, while the ordered ceramic structure altered the dynamics of the polymer chain segments at the ceramic/polymer interface, thereby improving ionic migration performance. However, these works lack conclusive evidence to fully explain the improved ion transport at the interface, and optimizing ion transport kinetics at the interface remains a challenge. Addressing this issue is crucial for extending the cycle life of vertically aligned CSEs and achieving stable cycling performance in solid-state batteries.

Recent research have shown significant interest in polyvinylidene fluoride (PVDF)-based ferroelectric copolymers, such as poly(vinylidene fluoride-*co*-trifluoroethylene) (P(VDF-TrFE)) and poly(vinylidene fluoride-*co*-trifluoroethylene-*co*-chlorofluoroethylene) (P(VDF-TrFE-CFE)), due to their high dielectric constants and reduced crystallinity [14]. These high-dielectric polymers offer significant advantages in promoting lithium salt dissociation, modulating ion transport pathways, and regulating interfacial charge distribution [15]. Residual dimethylformamide (DMF) can coordinate with Li^+ to form $[Li(DMF)_x]^+$ complexes, which could be transported through the PVDF matrix through interactions between the complexes and PVDF chains [16]. Moreover, the ion migration process is highly dependent on the spatial conformation of F atoms along the polymer chain, and a more ordered chain arrangement facilitates more efficient ion transport [17]. In addition, the ordered arrangement of PVDF molecular chains can effectively regulate the electric field distribution at the electrode|electrolyte interface, thereby preventing non-uniform lithium deposition and extending battery lifespan. Wei et al. [18] reported that inducing the conversion of PVDF to the *all-trans* (β-phase) can create an internal electric field between the polymer and lithium metal, significantly enhancing ion deposition in lithium metal batteries. Inducing such a phase transition in the PVDF copolymers is expected to further suppress the growth of lithium dendrites and improve the cycling stability of batteries. However, PVDF copolymers still face challenges such as low ionic conductivity at room temperature and interfacial side reactions when used as electrolytes, which hinder their further development [19].

In this work, $Li_{1.3}Al_{0.3}Ti_{1.7}(PO_4)_3$ (LATP), known for its high ionic conductivity and excellent chemical stability, was selected and combined with phase inversion and sintering processes to develop a novel CSE. This electrolyte features a three-dimensional support structure composed of vertically aligned LATP skeleton array within a polymer matrix of P(VDF-TrFE-CFE)/lithium bis(fluorosulfonyl)imide (LiFSI), referred to as 3D-LATP. This structure provides several key advantages: i) the LATP framework provides fast Li^+ transport "highways" with strong adsorption of DMF solvents, while offering robust structural support; ii) the polar P(VDF-TrFE-CFE) polymer, rich in β-phase content, significantly enhances lithium salt dissociation, accelerating the rapid Li^+ transport at the ceramic/polymer interface and providing an additional pathway for Li^+ transport; iii) the P(VDF-TrFE-CFE) polymer interlayer at the lithium metal|CSE interface generates a uniformly distributed electric field, facilitating uniform deposition of Li^+ and forming a dense solid electrolyte interphase (SEI) layer rich in LiF and Li_3N. The results demonstrate that the Li^+ transport efficiency of the 3D-LATP is significantly improved, compared to disordered CSE (denoted as 0D-LATP) and polymer electrolyte (denoted as PVTC). Furthermore, the Li|3D-LATP|Li symmetric cells allow for ultra-stable operation. The Li|3D-LATP|LFP full cells exhibit high specific discharge capacity and ultra-long cycle life at room temperature, with excellent capacity reversibility.

2. Results and discussion

2.1. Preparation and characterization of 3D-LATP, 0D-LATP and PVTC electrolytes

Digital photographs of all the electrolytes—3D-LATP, 0D-LATP and PVTC—are shown in **Fig. S1**. The incorporation of LATP ceramics imparts a white color to the transparent pure polymer electrolyte. To analyze the structural characteristics of 3D-LATP, surface and cross-sectional morphologies of the samples were examined by scanning electron microscopy (SEM). The cross-sectional view of the LATP ceramic framework, as shown in Fig. 1a, reveals an asymmetric structure composed of vertically aligned porous regions and a dense ceramic framework. The surface of the porous layer is interconnected with the interior framework, allowing for the infiltration polymers, while the dense layer serves as a barrier against the formation of lithium dendrite (**Fig. S2**a, b). After incorporating the polymer matrix, as shown in Fig. 1b and **S3**, the intimate contact between LATP and polymer virtually eliminates pores within the CSE. Energy dispersive X-ray spectroscopy (EDS) mapping results of Ti, N, and F elements further confirm the homogeneous distribution of polymer throughout the ceramic framework (Fig. 1c-e). In contrast, the 0D-LATP electrolyte shows a rough surface, with significant LATP particle agglomeration visible (**Fig. S4**a, b), when compared to the PVTC membrane (**Fig. S4**c, d). Fig. 1f demonstrates that the 3D-LATP exhibits flexibility without fracturing, indicating that this CSE reduces the inherent rigidity of LATP, forming a flexible structure capable of withstanding deformation. Thermal stability tests were also conducted by placing the electrolytes on lithium metal under heating, as illustrated in Fig. 1g. When raising the temperature to 300 °C, impressively, the 3D-LATP maintains remarkable structural integrity and does not react with lithium metal, confirming its excellent safety feature. In stark contrast, the 0D-LATP electrolyte explodes and catches fire, while the PVTC electrolyte experiences pronounced deformation. Thermogravimetric analysis (**Fig. S5**) reveals that all three samples contain only small amounts of residual DMF, specifically 3 wt% for PVTC, 2 wt% for 0D-LATP and 1.8 wt% for 3D-LATP. These similar residual levels suggest that DMF is unlikely to cause significant differences in their ionic conductivities.

Linear scanning voltammetry (LSV) curves were measured to determine the electrochemical stability window (ESW) of all electrolytes. According to Fig. 1h, the 3D-LATP electrolyte extends the ESW up to 4.78 V, notably, with no significant reduction peaks observed near 1.5 V. This suggests that the 3D-LATP electrolyte effectively suppresses the decomposition of DMF while demonstrating excellent electrochemical stability. In PVDF-based electrolytes, the Li^+ conduction occurs through interactions between the C-F bonds of PVDF and the DMF-Li salt complex [20]. Nevertheless, excessive freely mobile DMF solvents are detrimental to the Li metal|electrolyte interface [21]. Therefore, the affinity of DMF for LATP and PVDF polymers is subsequently evaluated using density functional theory (DFT) calculations. Fig. 1i-j and S6 show the adsorption of DMF on the most stable sites of the LATP (113) surface, and on two phases of PVDF. The results reveal that LATP has a significantly higher adsorption energy for DMF (−4.53 eV) compared to β-PVDF (−0.92 eV) and α-PVDF (0.03 eV), suggesting a strong preference for DMF adsorption on LATP. Large isosurfaces of charge difference due to DMF adsorption, as shown in Fig. 1k, also suggest the origins of strong adsorption, while for both α-/β-PVDF, there is little charge

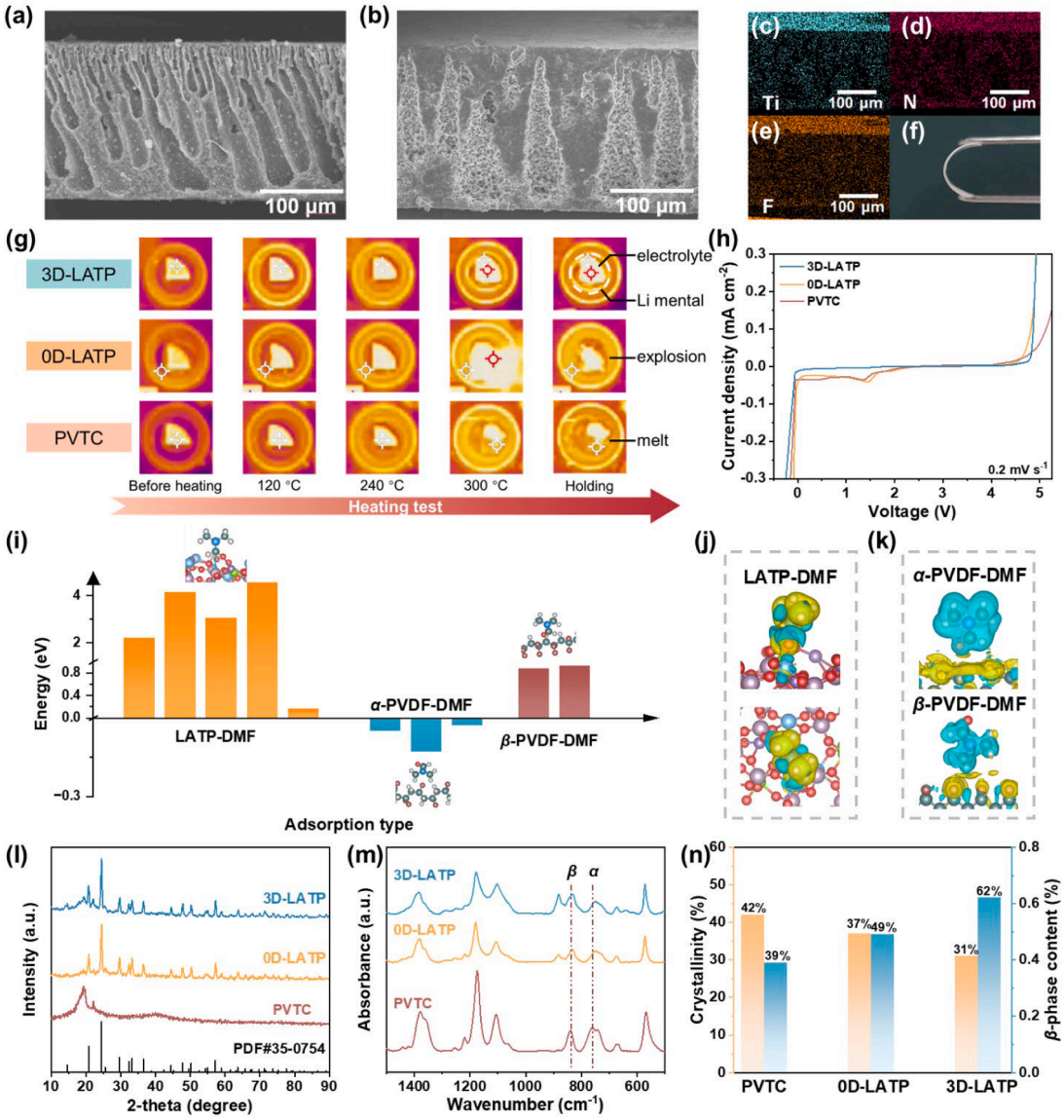

Fig. 1. Cross-sectional SEM image of (a) the 3D-LATP framework and (b) the 3D-LATP CSE. (c-e) EDS mapping results showing the elemental distributions of Ti, P, and F elements in the 3D-LATP CSE. (f) Digital photograph of bent 3D-LATP membrane. (g) Thermal stability tests of 3D-LATP, 0D-LATP and PVTC electrolytes against lithium metal in an argon-filled glove box. (h) Electrochemical stability window of 3D-LATP, 0D-LATP and PVTC electrolytes. (i) Adsorption energy of DMF on LATP (113) surface and on α-/β-phase of PVDF. (j) Side view and top view of calculated electron density difference before and after the adsorption of DMF on LATP surface. (k) Difference in electron density of DMF aggregation before and after adsorption on α-PVDF and β-PVDF, cyan and yellow isosurface (0.01 a.u.) represent electron depletion and accumulation, respectively. (l) XRD patterns, (m) FT-IR spectra, and (n) comparison in terms of crystallinity and β-phase variations of 3D-LATP, 0D-LATP and PVTC electrolytes.

transfer between the DMF molecules and the polymer. This strong interaction between LATP and DMF molecules can significantly extend the ESW of 3D-LATP electrolyte, which is well aligned with the superior reductivity of 3D-LATP as observed in Fig. 1j. During battery cycling process, the strong affinity of DMF for LATP results in its preferential adsorption onto LATP surface. This significantly enhances the transfer of dissociated Li^+ ions along the polymer/ceramic interface.

The phase structures of all electrolytes were detected using X-ray diffraction (XRD) (Fig. 1l). The results demonstrate that the diffraction peaks align closely with the standard NASICON structure of $LiTi_2(PO_4)_3$ (PDF #35-0754) [22], with no impurity phases detected. As illustrated in **Fig. S7**, crystallinity of polymer matrix derived from the XRD curves indicates that 3D-LATP exhibits the lowest crystallinity, suggesting that the vertically aligned LATP framework effectively enhances the mobility of chain segments of P(VDF-TrFE-CFE) within the CSE. The effect of LATP on P(VDF-TrFE-CFE) was further analyzed by Fourier transform infrared (FT-IR) spectroscopy (Fig. 1m). The α-phase and β-phase are two common crystalline configurations of PVDF [23]. The β-phase adopts an *all-trans* (TTTT) conformation and exhibits the highest polarity, which significantly enhances its dielectric properties [24]. Such a high polarity endows the PVDF-based polymer electrolytes with a high content of β-phase to facilitate lithium salt dissociation and promote the Li^+ migration within the electrolyte [25]. Conversely, the α-phase consists of alternating *trans* and *gauche* conformations (TGTG), where the dipole moments cancel each other, resulting in negligible polarization properties. According to the Beer-Lambert law (Equation (S1)), the β-phase content in the 3D-LATP electrolyte was calculated to be 62 %, significantly higher than that of 0D-LATP (49 %) and PVTC (39 %), respectively (Fig. 1n). The uniform arrangement of LATP in 3D-LATP is believed to induce a phase transition to the β-phase by interacting with the $-CF_2/-CH_2$ dipole in P(VDF-TrFE-CFE). In contrast, the uneven distribution and agglomeration of ceramic particles in the 0D-LATP

electrolyte reduces the proportion of TTTT conformations.

2.2. Investigations of Li^+ transport kinetics and mechanisms of 3D-LATP

To investigate the lithium-ion transport mechanism, a series of experiments, theory simulations, and finite element analyses were carried out. First, the temperature-dependent ionic conductivity and corresponding activation energies (E_a) derived from the Arrhenius equation (**Equation (S2)**) are presented in Fig. 2a. Specifically, at 25 °C, 3D-LATP exhibits the highest ionic conductivity (5.8×10^{-4} S cm^{-1}), which is 2.4 times higher than that of 0D-LATP (2.4×10^{-4} S cm^{-1}) and significantly higher than that of PVTC (7×10^{-5} S cm^{-1}). Notably, the 3D-LATP without liquid electrolyte exhibits a room-temperature ionic conductivity of 3.85×10^{-4} S cm^{-1} and a Li^+ transference number of 0.5 (**Fig. S9**), which clearly indicates that the intrinsic ion transport capability of the 3D-LATP is primarily governed by the continuous solid-state pathways formed by the vertically aligned LATP skeleton and the copolymer matrix. In addition, 3D-LATP achieves the lowest E_a of 0.3 eV, suggesting that Li^+ has the lowest diffusion barrier within this electrolyte. Compared to PVTC, the incorporation of inorganic ceramics reduces the crystallinity of polymers, resulting in improved ionic conductivity. The Li^+ transference number (t_{Li}^+) is another critical performance index for electrolytes. As shown in Fig. 2b and **S8**, the t_{Li}^+ of 3D-LATP is 0.56, much higher than that of 0D-LATP (0.3) and PVTC (0.13), determined according to the Bruce-Vincent-Evans method.

To explore the reasons behind the enhanced kinetics, Raman spectroscopy was first employed (Fig. 2c and **S10**). This analysis provides insights into how ion pairing and dissociation contribute to improved ionic conductivity and overall electrolyte performance. The PVTC electrolyte exhibits 32.0 % of contact ion pairs (CIP, 727 cm^{-1}), [26] 47.9 % of aggregated clusters, *i.e.*, AGGs-1 (one FSI^- coordinating two Li^+, near 734 cm^{-1}) and AGGs-2 (one FSI^- coordinating more than two Li^+, near 742 cm^{-1}), and only 19.9 % of free FSI^- (723 cm^{-1}) [27]. With the addition of ceramic LATP, the proportion of free FSI^- increases to 26.5 % (0D-LATP) and 38.8 % (3D-LATP). These findings confirm that the LATP framework greatly enhances ion cluster dissociation, boosting concentration of free Li-ions within the CSEs.

To further investigate the lithium mobility in polymer matrix, the

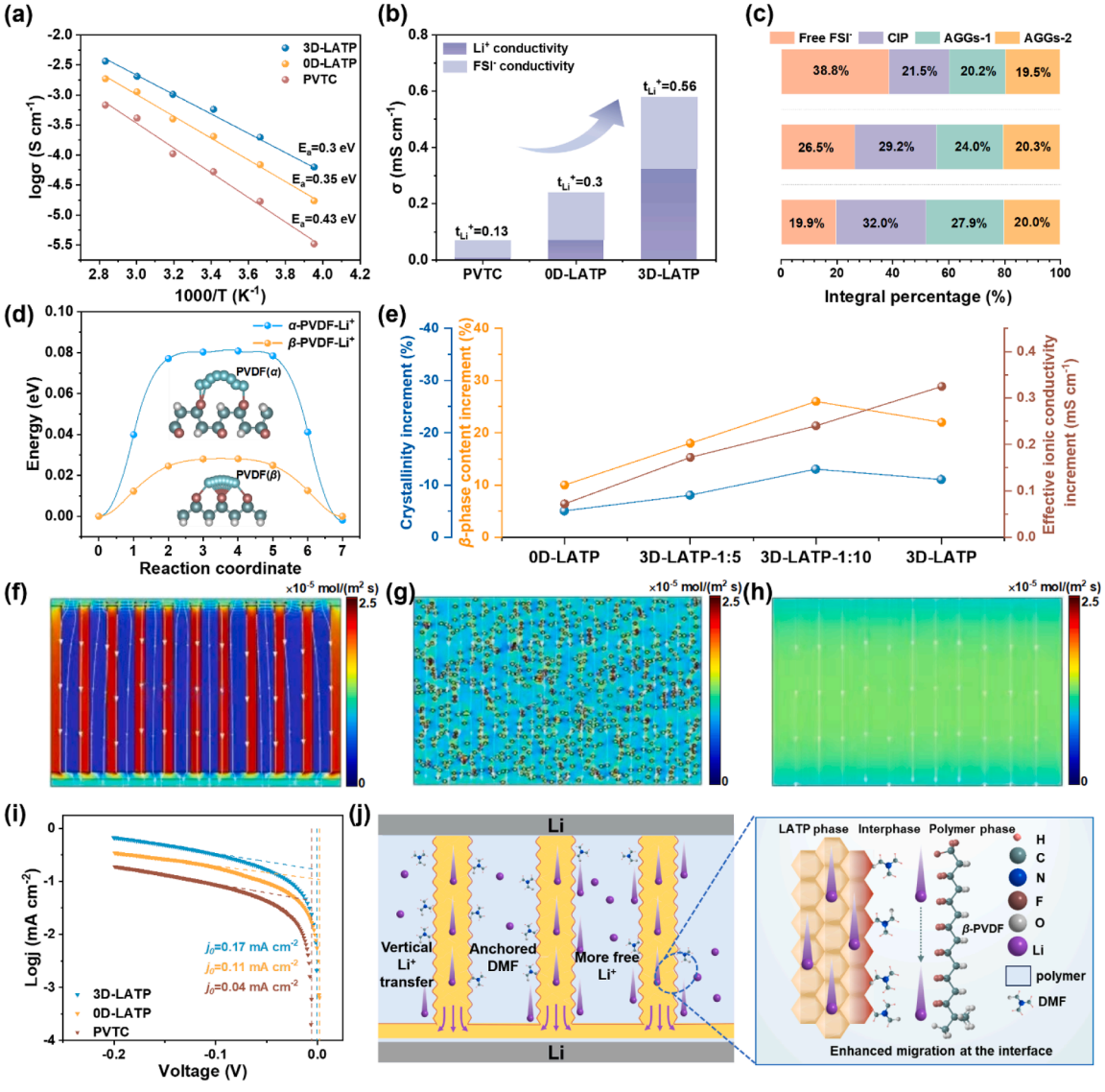

Fig. 2. (a) Temperature-dependent ionic conductivities, (b) Comparison of ionic conductivity and Li^+ transference number, and (c) Integral percentages derived from the Raman spectra for 3D-LATP, 0D-LATP, and PVTC electrolytes. (d) Migration paths and corresponding Li^+ diffusion barrier on α-/β-phases of PVDF. (e) Increment in crystallinity, β-phase content, and effective ionic conductivity of LATP-modified CSEs compared to PVTC. Li^+ fluxes within (f) 3D-LATP, (g) 0D-LATP and (h) PVTC based on COMSOL simulations. (i) Tafel plots of 3D-LATP, 0D-LATP, and PVTC electrolytes. (j) Schematic illustration of Li^+ transport mechanism in 3D-LATP.

climbing image nudged elastic band (CI-NEB) method was employed to determine the migration path (Fig. 2d). Six intermediate images were linearly interpolated between the most stable positions. For α-phase PVDF, CI-NEB calculations show that lithium-ions migrated from the top of one fluorine (F) atom to the nearest F atom, encountering a kinetic barrier of 0.08 eV, with the saddle point located on top of a carbon (C) atom. For β-phase PVDF, lithium-ions migrate from the top of a C atom to the nearest carbon atom, facing a smaller kinetic barrier of 0.03 eV, with the saddle point situated on top of a F atom. This comparison of diffusion energy barriers in the two PVDF crystalline phases indicates that Li^+ diffuses faster in the β-phase PVDF, aligning well with experimental observations.

To better reflect the actual composition, we refer to the samples based on the PVB:LATP mass ratios used in fabrication. Frameworks designated as 3D-LATP-1:5 were obtained using 0.1 g of PVB and 0.5 g of LATP, while 3D-LATP-2:5 frameworks were prepared using 0.2 g of PVB and 0.5 g of LATP (**Fig. S11**). Thermal decomposition of PVB during sintering is believed to influence the specific surface area of the LATP framework. Higher PVB content promotes the formation of a larger specific surface area, thereby enhancing interfacial contact with the polymer. Fig. 2e presents the trend of crystallinity, β-phase content, and effective ionic conductivity of LATP-modified CSEs, with respect to the PVTC electrolyte, derived from **Table S1**. It is revealed that the incorporation of LATP ceramic induces reduced crystallinity and increased β-phase content. As the ceramic/polymer interfacial surface area increases, the crystallinity further decreases while the β-phase content significantly rises (**Fig. S12-S13**). This leads to a notable improvement in the effective ionic conductivity of the CSEs (**Fig. S14-S15**). However, the 3D-LATP-2:5 CSE, despite having a higher specific surface area, fails to further enhance the ionic conductivity. This could be attributed to the excessive PVB content disrupting the connectivity of the LATP framework, emphasizing that maintaining LATP connectivity is crucial for preserving the superionic conductor properties of bulk LATP and thereby enhancing effective ionic conductivity.

To deepen the analysis of lithium-ion transport in various electrolytes, COMSOL was adopted to model the Li^+ concentration in 3D-LATP, 0D-LATP, and PVTC, using simplified two-dimensional structures, respectively. Evident from Fig. 2f-h, both 3D-LATP and 0D-LATP exhibit higher Li^+ fluxes in the ceramic region, with 3D-LATP providing a continuous and wider ceramic pathway, resulting in significantly higher Li^+ flux. Tafel curves (Fig. 2i) show that the Li|3D-LATP|Li cell exhibits a j_0 of 0.17 mA cm^{-2}, significantly higher than the Li|0D-LATP|Li cell (j_0 = 0.11 mA cm^{-2}) and the Li|PVTC|Li cell (j_0 = 0.04 mA cm^{-2}). This suggests that a more kinetically favorable charge transfer interface is formed for ion transport between Li metal and 3D-LATP.

Collectively (Fig. 2j), the construction of vertically aligned LATP arrays plays an important role in anchoring mobile DMF solvents, which promotes the migration of dissociated Li^+ toward the ceramic/polymer interface and enhances ion transport. Meanwhile, the formation of vertically aligned, dense LATP arrays, achieved by balancing the ceramic/polymer interface area while maintaining the dense structure of LATP, successfully induces abundant β-phase content to promote the dissociation of lithium salts. Additionally, it significantly reduces polymer's crystallinity, thereby enhancing Li-ion migration, and more importantly, enables the creation of continuous and shortened Li^+-conductive "highways", further accelerating Li^+ transport kinetics. These findings reveal that 3D-LATP not only supports rapid ionic conduction within the ceramic framework, but also establishes additional ionic conduction pathways at the ceramic/polymer interfaces. As a result, 3D-LATP achieves pronouncedly higher ionic conductivity compared to 0D-LATP despite the same ceramic content.

2.3. Mechanistic investigation of enhanced cyclability in Li||Li cells

The Li||Li symmetric cells were assembled to evaluate the capability of various electrolytes in inhibiting Li dendrites formation. Critical current density (CCD) tests were performed, with the results demonstrated in Fig. 3a and 3b. Under the time-constant mode, it is noteworthy that 3D-LATP could withstand current densities up to 1.3 mA cm^{-2}, significantly outperforming 0D-LATP and PVTC, which exhibit much lower CCD values, *i.e.*, 0.45 mA cm^{-2} and 0.35 mA cm^{-2}, respectively. Switching to the capacity-constant mode with a fixed capacity of 0.3 mAh cm^{-2}, a similar trend is evidenced, with CCD values following the order of 3D-LATP (3 mA cm^{-2}) > 0D-LATP (1.6 mA cm^{-2}) > PVTC (0.9 mA cm^{-2}). To assess the long-term interfacial stability, lithium stripping-plating experiments were conducted at 0.3 mA(h) cm^{-2} (Fig. 3c). Specifically, PVTC-based symmetric cells could not withstand such a high current density, leading to cell short-circuit after only 34 h of cycling. The addition of disorderly dispersed LATP filler prolongs the cycle life to 93 h. In sharp contrast, the Li|3D-LATP|Li cells are capable of cycling stably for 1500 h without significant degradation. Additionally, 3D-LATP allows lithium symmetric cells to cycle over 600 h at 0.5 mA(h) cm^{-2} (Fig. 3d) and over 3000 h at 0.1 mA(h) cm^{-2} (**Fig. S16**). These results collectively demonstrate the impressive stability of 3D-LATP against Li metal.

The *ex situ* morphology and elemental composition of cycled lithium metal electrodes were analyzed to understand the superior cycling stability of 3D-LATP against lithium anode. After cycling, lithium symmetric cells were disassembled to examine the surface and cross-sectional morphologies of cycled lithium metal. As presented in Fig. 3e-f and **Fig. S17**, Li metal deposition is inhomogeneous in the Li|PVTC|Li cell, resulting in a rough and loosely packed layer of reactive/dead lithium. The cycled lithium metal recovered from the Li|0D-LATP|Li cell shows a porous/dead lithium layer with a thickness of approximately 50 μm. On the contrary, using 3D-LATP results in the lithium metal surface to be much more compact, with a significantly reduced thickness of approximately 16 μm and no lithium dendrite formation. These findings suggest that the 3D-LATP significantly mitigates the interfacial side reactions between lithium metal and the electrolyte, contributing to enhanced interface stability and improved electrochemical performance.

Subsequently, *ex situ* X-ray photoelectron spectroscopy (XPS) analyses of the SEI layer on cycled Li metals were investigated to further understand the interfacial chemistry with varying electrolytes (Fig. 4g-h and **Fig. S18**). The XP peaks of C—C (284.8 eV), C—H (286.1 eV), and C-F (290.6 eV) (**Fig. S18**(a)), [28] are attributed to the decomposed products of the P(VDF-TrFE-CFE) polymer. The C=O peak at 288.8 eV is ascribed to the decomposition of N—C=O groups in DMF [29]. The significantly stronger C=O signal in the PVTC-based cell confirms that DMF anchored in the 3D-LATP electrolyte plays a crucial role in enhancing interfacial electrochemical stability. The Li 1 s XP spectra show peaks corresponding to LiF (54.5 eV), Li_3N (55 eV), and LiOH (56.5 eV), which result from the decomposition of FSI^- and DMF [30]. From the F 1 s XP spectra, the 0D-LATP exhibits much higher LiF content compared to the other two systems. This is correlated with the rough lithium surface and loose deposit's morphology observed in 0D-LATP, which likely results from the excessive decomposition of LiFSI leading to continuous SEI reconstruction. Furthermore, this process consumes lithium salts and hinders Li^+ transport during cycling, ultimately causing battery failure. The 3D-LATP facilitates the formation of a hybrid SEI with rather high concentrations of Li_3N and LiF, both favorable for Li^+ transport while blocking electron transport, thereby contributing to a stable lithium interface [31].

Considering the different polymer β-phase existing in the electrolytes, finite element COMSOL simulations were conducted to study the electric field strength and electric potential distributions at the Li|electrolyte interface through regulating the dielectric constants of polymers. The simulations aim to understand how differences in β-phase, which contributes to the dielectric properties of the polymer matrix, influence lithium-ion transport and Li deposition behavior (Video S1-S3). At the Li|PVTC interface, the electric field strength is highly concentrated at the lithium metal protrusions, attracting Li^+ and leading to continuous

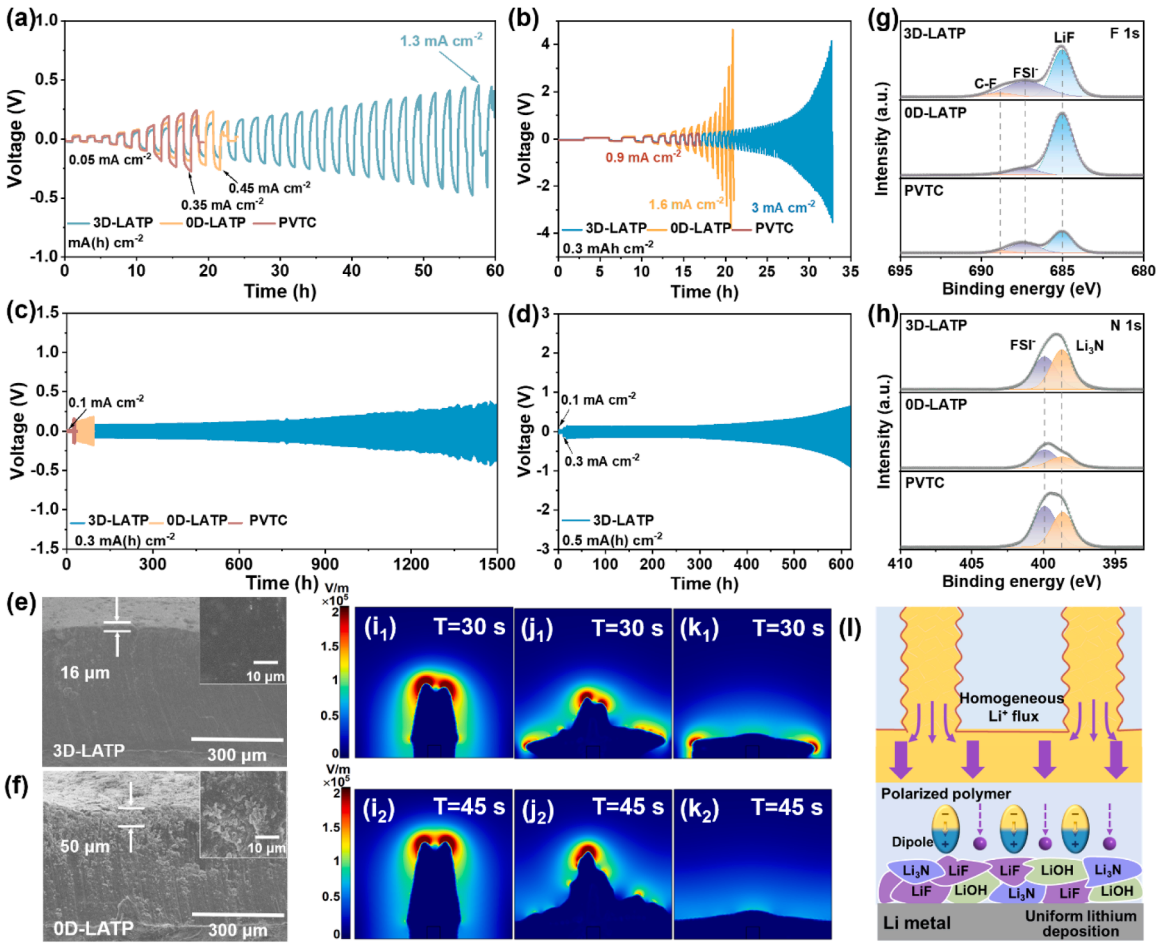

Fig. 3. Evaluation of critical current densities using (a) time-constant and (b) capacity-constant mode for 3D-LATP, 0D-LATP and PVTC electrolytes. Lithium stripping-plating curves of Li||Li symmetric cells at (c) 0.3 mA(h) cm^{-2}. and (d) 0.5 mA(h) cm^{-2}. *Ex situ* morphology examination of cycled Li metal anodes recovered from Li||Li symmetric cells using (e) 0D-LATP and (f) 3D-LATP as the electrolyte. *Ex situ* XP spectra of (g) F 1 s and (h) N 1 s of cycled Li metals. Electric field strength simulations at the interface of (i) Li|PVTC, (j) Li|0D-LATP, and (k) Li|3D-LATP at 30 s and 45 s. (l) Schematic illustration of lithium deposition mechanism at the Li|3D-LATP interface.

and uneven deposition, fostering dendrite growth (Fig. 3i_1 and 3i_2). For the Li|0D-LATP interface, the electric field strength focuses at the top and sides of the Li metal, promoting inhomogeneous deposition and causing continuous thickening of the SEI film (Fig. 3j_1 and 3j_2), further aggravating the irregular Li deposition. In contrast, as shown in Fig. 3k_1 and Fig. 3k_2, the Li|3D-LATP interface achieves considerably more uniform electric field strength distribution, highlighting its distinct advantage of the highest dielectric constant which facilitates lateral Li deposition and mitigates risks associated with Li^+ concentration gradients. The electric potential field simulations illustrate the lithium dendrite pattern at the interface of different samples, further indicating that a high dielectric constant promotes uniform Li deposition and a more homogeneous potential distribution (Fig. 3l and **S19**).

2.4. Evaluation of electrochemical performance in full cells

Li||$LiFePO_4$ (LFP) full cells were assembled and tested at 25 °C to assess the rate and cycling performance when using the three investigated electrolytes. The rate capability of the cells are compared in Fig. 4a, while Fig. 4b and **S20** display the dis-/charge voltage curves of Li|3D-LATP|LFP cells at varying C-rates. The Li|3D-LATP|LFP cell delivers specific discharge capacities of 162, 155, 139, 128, 107, and 84 mAh g^{-1}, at 0.1, 0.2, 0.5, 1, 2, and 5 C, respectively. When the C-rate returns to 0.1 C, a fully reversible capacity of 161 mAh g^{-1} is recovered, showcasing its excellent reversibility. In contrast, the Li|0D-LATP|LFP cell shows a rapid capacity drop from 2 C onward, while the Li|PVTC|LFP cell does not operate at 5 C. These results highlight the superior rate performance of Li|3D-LATP|LFP mainly deriving from the efficient ion transport and low interfacial impedance.

Fig. 4c demonstrates the long-term cycling performance of the Li||LFP full cells at 1 C. Following the activation cycle, performed at 0.1 C rate, the Li|3D-LATP|LFP cell demonstrates an ultra-long cycle life, retaining 90 % and 80 % capacity of its initial capacity after 1400 and 2500 cycles, respectively, with an average Coulombic efficiency exceeding 99.7 %. In contrast, the Li|0D-LATP|LFP cell experiences significant capacity degradation and fails after 300 cycles (**Fig. S21**b), while the Li|PVTC|LFP cell only completes 50 cycles at 1 C due to the lack of mechanical support from the PVTC electrolyte (**Fig. S21**c). The average voltage difference between charge and discharge plateaus serves as an indicator of the polarization level within a cell. For the Li|3D-LATP|LFP full cell, as shown in Fig. 4d, this voltage difference is measured at 0.126 V and remains stable throughout cycling, indicating for high reversibility and minimal polarization. This latter is primarily attributed to the high effective ionic conductivity of the 3D-LATP electrolyte and the significantly mitigated interfacial side reactions. The stability in voltage difference further confirms the remarkable efficiency of 3D-LATP in facilitating ion transport, contributing to the cell's long-term performance and reduced energy losses during cycling. Increasing the C-rate to 2 C, the Li|3D-LATP|LFP cell still exhibits promising cycling performance, retaining 76 % of its capacity after 1500 cycles at 25 °C

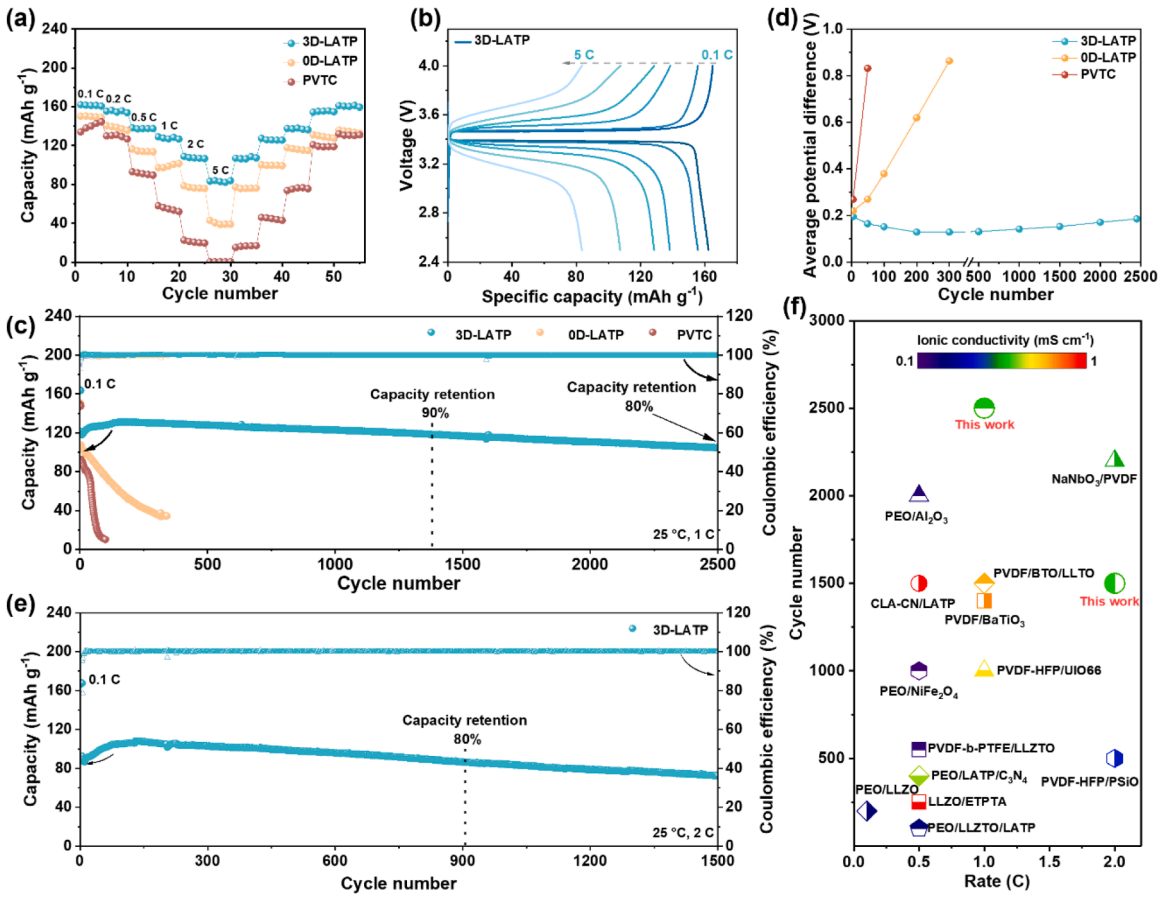

Fig. 4. (a) Rate performance of Li|3D-LATP|LFP, Li|0D-LATP|LFP, and Li|PVTC|LFP full cells. (b) Selected dis-/charge voltage profiles of Li|3D-LATP|LFP full cells. (c) Cycling performance of the three full cells at 1 C. (d) Evolution of average potential difference upon cycling at 1 C rate of Li|3D-LATP|LFP, Li|0D-LATP|LFP, and Li|PVTC|LFP full cells. (e) Long-term cycling performance of Li|3D-LATP|LFP cell at 2 C. (f) Comparison of the electrochemical performance with other recently reported lithium metal batteries using composite solid-state electrolytes.

(Fig. 4e). Elevating the mass loading of LFP cathode to 4.5 mg cm^{-2} (**Fig. S22**), the full cell still allows for stable cycling performance via maintaining 85 % capacity after 130 cycles at 0.5 C. Furthermore, when coupled with a high-mass-loading cathode (~20 mg cm^{-2}), the Li|3D-LATP|LFP cell delivers a high specific discharge capacity of 149.2 mAh g^{-1}, retaining 91.2 % of its initial capacity (137.1 mAh g^{-1}) at 0.2 C over 60 cycles (**Fig. S23**). These results highlight the enhanced ion transport efficiency provided by the vertical structure of the 3D-LATP CSE and confirm its excellent compatibility with high-mass-loading cathodes. A detailed comparison of recently reported solid-state lithium metal batteries using oxide-based ceramic electrolytes is presented in Fig. 4f and **Table S2**. This comparison highlights that the Li|3D-LATP|LFP cells achieve among the highest performance CSE-based batteries, showcasing promising potential for high-performance solid-state battery applications.

3. Conclusion

In this work, 3D-LATP composite solid-state electrolytes were successfully fabricated by infusing P(VDF-TrFE-CFE)-LiFSI polymer electrolytes into a vertically aligned LATP ceramic framework obtained by phase inversion method. The vertically aligned structure plays a crucial role by providing efficient ion transport "highways" and offering robust mechanical support. Furthermore, strong interactions between the LATP framework and DMF molecules facilitate improved ion migration at the interface and enhance the electrochemical stability with lithium metal anode. The high β-phase content in the P(VDF-TrFE-CFE) polymer, induced by such method, enhances ionic conduction not only in the bulk but also at the ceramic/polymer interface, via reducing the Li^+ diffusion energy barrier and promoting Li-salt dissociation, with the latter providing additional ion conduction channels. Additionally, the dipole-oriented alignment of P(VDF-TrFE-CFE) polymer generates a uniform internal electric field, which ensures even lithium deposition, preventing dendrite formation and promoting a dense and smooth interfacial layer on lithium anode surface. Collectively, the CSEs developed in this work, featuring with vertically interconnected structure, take advantages of the combined merits of ceramics and polymers, consequently creating a flexible, safe, and highly conductive electrolyte that supports stable and fast lithium-ion transport. As a result, the Li|3D-LATP|LFP full cells demonstrate remarkable performance, retaining 80 % of its initial capacity after 2500 cycles at 1 C. This design strategy for the 3D-LATP CSE presents a promising approach for developing high-performance, safe, long-lasting solid-state lithium metal batteries with excellent interfacial stability.

CRediT authorship contribution statement

Zeyu Niu: Writing – original draft, Investigation, Formal analysis, Data curation, Conceptualization. **Yuxuan Wang:** Visualization, Software, Data curation. **Yang Wang:** Writing – original draft, Investigation, Formal analysis. **Yixin Wu:** Investigation, Data curation. **Ziqi Zhao:** Formal analysis, Data curation. **Guanghui Li:** Investigation. **Jae-Kwang Kim:** Writing – review & editing, Formal analysis. **Xin Liu:** Project administration, Funding acquisition. **Zexiang Shen:** Writing – review & editing, Supervision. **Minghua Chen:** Supervision, Project administration, Conceptualization. **Stefano Passerini:** Writing – review & editing,

Conceptualization. **Zhen Chen:** Supervision, Project administration, Funding acquisition, Conceptualization.

Declaration of competing interest

The authors declare that they have no known competing financial interests or personal relationships that could have appeared to influence the work reported in this paper.

Acknowledgments

This work is supported by the National Natural Science Foundation of China (Grant No. 52277215, 52307237, 52377206), the Shandong Provincial Natural Science Foundation for Young Scholars (No. ZR2024QE011), the Postdoctoral Science Foundation of China (No. 2023M730884), and the Postdoctoral Science Foundation of Heilongjiang Province of China (LBH. Z23024, Z23198). We appreciate SuanChou (suanchou.com) for the phase-field model. S.P. acknowledges the basic funding from the Helmotz Association.

Supplementary materials

Supplementary material associated with this article can be found, in the online version, at doi:10.1016/j.ensm.2025.104492.

Data availability

Data will be made available on request.

References

[1] Y. Luo, X. Yang, C. Wang, A. Fraser, H. Zhang, X. Sun, X. Li, Advanced metal anodes and their interface design toward safe metal batteries: a comprehensive review, Prog. Mater. Sci. 139 (2023) 101171, https://doi.org/10.1016/j.pmatsci.2023.101171.

[2] G. Zubi, R. Dufo-López, M. Carvalho, G. Pasaoglu, The lithium-ion battery: state of the art and future perspectives, Renew. Sust. Energ. Rev. 89 (2018) 292–308, https://doi.org/10.1016/j.rser.2018.03.002.

[3] R. Sun, R. Zhu, J. Li, Z. Wang, Y. Zhu, L. Yin, C. Wang, R. Wang, Z. Zhang, The synergy mechanism of $CsSnI_3$ and LiTFSI enhancing the electrochemical performance of PEO-based solid-state batteries, Carbon Neutraliz. 3 (4) (2024) 597–605, https://doi.org/10.1002/cnl2.134.

[4] Z. Huang, M. Jing, P. Wang, W. Shao, Z. Zhang, G. Zhang, X. Shen, A high ionic conductive PDOL/LAGP composite solid electrolyte film for interfacial stable solid-state lithium batteries, Ceram. Int. 49 (3) (2023) 5510–5517, https://doi.org/10.1016/j.ceramint.2022.10.074.

[5] L. Zhong, J. Li, Z. Chen, L. Zhou, H. Liu, X. Shen, M. Jing, A LLZO fibers/PPO polymeric matrix solid electrolyte for high voltage solid-state lithium batteries, Appl. Phys. A 130 (2024) 202407815, https://doi.org/10.1007/s00339-024-07815-x.

[6] S. Li, S. Zhang, L. Shen, Q. Liu, J. Ma, W. Lv, Y. He, Q. Yang, Progress and perspective of ceramic/polymer composite solid electrolytes for lithium batteries, Adv. Sci. 7 (5) (2020) 201903088, https://doi.org/10.1002/advs.201903088.

[7] P. Fan, H. Liu, V. Marosz, N. Samuels, S. Suib, L. Sun, L. Liao, High performance composite polymer electrolytes for lithium-ion batteries, Adv. Funct. Mater. 31 (23) (2021) 202101380, https://doi.org/10.1002/adfm.202101380.

[8] R. Sahore, B. Armstrong, X. Tang, C. Liu, K. Owensby, S. Kalnaus, X. Chen, Role of scaffold architecture and excess surface polymer layers in a 3D-interconnected ceramic/polymer composite electrolyte, Adv. Energy Mater. 13 (19) (2023) 202203663, https://doi.org/10.1002/aenm.202203663.

[9] J. Sun, C. Liu, H. Liu, J. Li, P. Zheng, Y. Zheng, Z. Liu, Advances in ordered architecture design of composite solid electrolytes for solid-state lithium batteries, Chem. Rec. 23 (6) (2023) e202300044, https://doi.org/10.1002/tcr.202300044.

[10] G. Shao, D.A.H. Hanaor, X. Shen, A. Gurlo, Freeze casting: from low-dimensional building blocks to aligned porous structures-a review of novel materials, methods, and applications, Adv. Mater. 32 (17) (2020) 201907176, https://doi.org/10.1002/adma.201907176.

[11] Y. Chen, Y. Wu, Y. Liao, Z. Zhang, S. Luo, L. Li, Y. Wu, Y. Qing, Tuning carbonized wood fiber via sacrificial template-assisted hydrothermal synthesis for high-performance lithium/sodium-ion batteries, J. Power. Sources. 546 (2022) 231993, https://doi.org/10.1016/j.jpowsour.2022.231993.

[12] M. Lira, N. Kostretsova, I. Babeli, L. Bernadet, S. Marquez, A. Morata, M. Torrell, A. Tarancón, Large-area 3D printed electrolyte-supported reversible solid oxide cells, Electrochim. Acta 467 (2023) 143074, https://doi.org/10.1016/j.electacta.2023.143074.

[13] H. Zhang, X. An, Y. Yang, Y. Long, S. Nie, L. Liu, G. Yang, Z. Tian, H. Cao, Z. Cheng, H. Liu, Y. Ni, Vertical aligned solid-state electrolyte templated by nanostructured "upright" cellulose film layers for advanced cell performance, EcoMat 5 (4) (2023) e12317, https://doi.org/10.1002/eom2.12317.

[14] Y. Huang, J. Zeng, S. Li, C. Dai, J. Liu, C. Liu, Y. He, Conformational regulation of dielectric poly(vinylidene fluoride)-based solid-state electrolytes for efficient lithium salt dissociation and lithium-ion transportation, Adv. Energy Mater. 13 (15) (2023) 2203888, https://doi.org/10.1002/aenm.202203888.

[15] J. Barbosa, R. Pinto, D. Correia, A. Fidalgo-Marijuan, M. Silva, R. Gonçalves, S. Lanceros-Mendez, C. Costa, Effect of fluorinated polymer matrix type in the performance of solid polymer electrolytes based on ionic liquids for solid-state lithium-ion batteries, Chem. Eng. J. 478 (2023) 147388, https://doi.org/10.1016/j.cej.2023.147388.

[16] Q. Liu, G. Yang, X. Li, S. Zhang, R. Chen, X. Wang, Y. Gao, Z. Wang, L. Chen, Polymer electrolytes based on interactions between solvent-Li^+ complex and solvent-modified polymer, Energy Storage Mater. 51 (2022) 443–452, https://doi.org/10.1016/j.ensm.2022.06.040.

[17] Y. Huang, T. Gu, G. Rui, P. Shi, W. Fu, L. Chen, X. Liu, J. Zeng, B. Kang, Z. Yan, F. Stadler, L. Zhu, F. Kang, Y. He, A relaxor ferroelectric polymer with an ultrahigh dielectric constant largely promotes the dissociation of lithium salts to achieve high ionic conductivity, Energy Env. Sci. 14 (11) (2021) 6021–6029, https://doi.org/10.1039/d1ee02663a.

[18] W. Wang, L. Ma, B. Xu, H. Zhu, C. Zhang, L. Chen, W. Wei, Hydrogen bond boosted ferroelectric polarization enables high rate capability lithium metal batteries, Small. 20 (2) (2024) 202305797, https://doi.org/10.1002/smll.202305797.

[19] J. Zhu, S. He, H. Tian, Y. Hu, C. Xin, X. Xie, L. Zhang, J. Gao, S. Hao, W. Zhou, L. Zhang, The influences of DMF content in composite polymer electrolytes on Li^+-conductivity and interfacial stability with Li-metal, Adv. Funct. Mater. 33 (25) (2023) 202301165, https://doi.org/10.1002/adfm.202301165.

[20] P. Shi, J. Ma, M. Liu, S. Guo, Y. Huang, S. Wang, L. Zhang, L. Chen, K. Yang, X. Liu, Y. Li, X. An, D. Zhang, X. Cheng, Q. Li, W. Lv, G. Zhong, Y. He, F. Kang, A dielectric electrolyte composite with high lithium-ion conductivity for high-voltage solid-state lithium metal batteries, Nat. Nanotechnol. 18 (6) (2023) 602–610, https://doi.org/10.1038/s41565-023-01341-2.

[21] N. Zhu, J. Zhou, L. Zhang, N. Yao, D. Dastan, J. Zhang, Y. Chen, X. Zhang, Design and characterization of molecular, crystal and interfacial structures of PVDF-based dielectric nanocomposites for electric energy storage, Soft. Matter. 19 (24) (2023) 4401–4431, https://doi.org/10.1039/d3sm00291h.

[22] K. Kwatek, W. Slubowska, J. Trébosc, O. Lafon, J. Nowinski, Structural and electrical properties of ceramic Li-ion conductors based on $Li_{1.3}Al_{0.3}Ti_{1.7}(PO_4)_3$-LiF, J. Eur. Ceram. Soc. 40 (2020) 85–93, https://doi.org/10.1016/j.jeurceramsoc.2019.08.032.

[23] X. Cai, T. Lei, D. Sun, L. Lin, A critical analysis of the α, β and γ phases in poly (vinylidene fluoride) using FTIR, RSC. Adv. 7 (25) (2017) 15382–15389, https://doi.org/10.1039/c7ra01267e.

[24] J. Liu, Z. Wu, F. Stadler, Y. Huang, High dielectric poly(vinylidene fluoride)-based polymer enables uniform lithium-ion transport in solid-state ionogel electrolytes, Angew. Chem.-Int. Ed. 62 (26) (2023) e202300243, https://doi.org/10.1002/anie.202300243.

[25] Q. Wu, M. Fang, S. Jiao, S. Li, S. Zhang, Z. Shen, S. Mao, J. Mao, J. Zhang, Y. Tan, K. Shen, J. Lv, W. Hu, Y. He, Y. Lu, Phase regulation enabling dense polymer-based composite electrolytes for solid-state lithium metal batteries, Nat. Commun. 14 (2023) 6296, https://doi.org/10.1038/s41467-023-41808-3.

[26] J. Ding, R. Xu, N. Yao, X. Chen, Y. Xiao, Y. Yao, C. Yan, J. Xie, J. Huang, Non-solvating and low-dielectricity cosolvent for anion-derived solid electrolyte interphases in lithium metal batteries, Angew. Chem.-Int. Ed. 60 (20) (2021) 11442–11447, https://doi.org/10.1002/anie.202101627.

[27] X. An, Y. Liu, K. Yang, J. Mi, J. Ma, D. Zhang, L. Chen, X. Liu, S. Guo, Y. Li, Y. Ma, M. Liu, Y. He, F. Kang, Dielectric filler-induced hybrid interphase enabling robust solid-state Li metal batteries at high areal capacity, Adv. Mater. 36 (13) (2024) 2311195, https://doi.org/10.1002/adma.202311195.

[28] W. Yang, Y. Liu, X. Sun, Z. He, P. He, H. Zhou, Solvation-tailored PVDF-based solid-state electrolyte for high-voltage lithium metal batteries, Angew. Chem.-Int. Ed. 63 (18) (2024) e202401428, https://doi.org/10.1002/anie.202401428.

[29] Y. Liang, J. Zhang, S. Guan, K. Wen, C. Guo, Y. Wu, H. Yuan, S. Liu, Y. Qi, W. Mo, X. Zhang, C. Nan, Modification of solid electrolyte interface layer between PVDF-based electrolyte and lithium anode, J. Mater. 10 (4) (2024) 880–888, https://doi.org/10.1016/j.jmat.2023.12.003.

[30] G. Eshetu, T. Diemant, S. Grugeon, R. Behm, S. Laruelle, M. Armand, S. Passerini, In-depth interfacial chemistry and reactivity focused investigation of lithium-imide- and lithium-imidazole-based electrolytes, ACS. Appl. Mater. Interfaces. 8 (25) (2016) 16087–16100, https://doi.org/10.1021/acsami.6b04406.

[31] J. Li, L. Zhong, J. Li, H. Wu, W. Shao, P. Wang, M. Liu, G. Zhang, M. Jing, Insights into the effects of different inorganic fillers on the electrochemical performances of polymer solid electrolytes, Colloid Surf. A-Physicochem. Eng. Asp. 671 (2023) 131704, https://doi.org/10.1016/j.colsurfa.2023.131704.